Insights into the bonding properties and magnetism of the Mn-B system with a physically constrained neural network functional

Chao Zhou,[1] Kuo Bao,[1,*] Zekun Yu,[1] Jinming Zhu,[1] Hongyu Yu,[1] and Tian Cui[2,1,†]
[1]*State Key Laboratory of Superhard Materials, College of Physics, Jilin University, Changchun 130012, China*
[2]*Institute of High Pressure Physics, School of Physical Science and Technology, Ningbo University, Ningbo 315211, People's Republic of China*

(Received 21 April 2024; revised 19 July 2024; accepted 19 August 2024; published 6 September 2024; corrected 2 October 2024)

In this study, we explore the manganese borides (Mn-B) system, chiefly on its complex magnetic properties that are of extensive academic interest and of significant potential for applications in magnetism. We employed an approach by using a machine-learning trained, physically constrained neural network functional to reevaluate the Mn-B system comprehensively. This offers insights into several contentious aspects of the system from an enthalpy perspective, including the spin frustration in Mn_2B, the ground state of MnB_2, and the ongoing debates about the synthesis and various phases of MnB and MnB_4. Additionally, we establish a nearly linear relationship between the bonding strength and measured hardness in borides, which enhances the understanding of their mechanical properties with our proposed descriptor of bonding strength. Spin dynamics predictions highlight both discrepancies and consistencies related to the itinerant characteristics of magnetic moments, primarily driven by a high density of states of the magnetic atoms at the Fermi level (E_F). This suggests that traditional local-moment models may be inadequate for describing these itinerant magnetic systems. This work provides insight for understanding the bonding properties and magnetism of magnetic intermetallic compounds.

DOI: 10.1103/PhysRevB.110.094411

I. INTRODUCTION

Transition-metal borides (TMBs) are renowned for their high melting points, hardness, electrical and thermal conductivities, and occasionally magnetic properties [1]. Moreover, they hold significant potential as two-dimensional or nanomaterials, as well as other possible functional materials, with extensive applications [2–5]. Among these TMBs, the combination of boron with manganese (Mn), which possesses the maximum number of unpaired d electrons, would exhibit many novel properties. Based on early research [6,7] and the recent systematic synthesis work on the Mn-B binary system under high-pressure and high-temperature (HPHT) methods conducted by Ma *et al.* [8–13], the most commonly synthesized phases in the Mn-B system include Mn_2B, MnB, Mn_3B_4, MnB_2, and MnB_4, all of which exhibit rich mechanical and magnetic properties. The analysis of their structures revealed that as the boron content increases, the boron atoms in these systems tend to form chains, networks, or three-dimensional frameworks. The experimental synthesis of the manganese borides is approaching maturity, and numerous related predictive studies were already conducted [14–17]. However, there remain significant controversies within this system. For instance, Aydin *et al.* predicted that ReB_2-type MnB_2 could be a superhard material for its predicted extremely high hardness [18]. Subsequently, Wang *et al.* also predicted ReB_2-type MnB_2 to be a thermodynamically stable phase, which suggested that it could be synthesized experimentally [14]. But, Gou *et al.* synthesized AlB_2-type MnB_2 and used the $+U$ method to study its great stability [19]. Subsequently, Niu *et al.* determined that ReB_2-type MnB_2 lies on the convex hull and observed that the $+U$ method predicts a larger magnetic moment for this compound compared to the experimental findings for AlB_2-type MnB_2 [15]. Another theoretical study suggested that high temperature above 1020 K is necessary to synthesize ReB_2-type MnB_2 [20], but only the AlB_2-type MnB_2 was synthesized in the HTHP experimental attempts with the temperature above 1900 K [8]. It is important to note that manganese borides are studied for both their mechanical and magnetic properties on the contributions of boron and manganese, respectively. Kaner *et al.* proposed in 2005 that transition-metal borides might be superhard [21], and comparable traditional covalent crystals. However, to date, no convincing superhard materials have been confirmed in TMBs [3]. Many studies explored the mechanical properties of manganese borides [8–13,22]. Gou *et al.* initially measured the hardness of $mP20$-MnB_4 as high as 34.6 GPa [22], while Ma *et al.* measured the hardness $oP10$-MnB_4 as 20.1 GPa, which is the highest among the manganese borides they synthesized [8–13]. However, theoretical estimates place the hardness of MnB_4 at 38.7 or 49.9 GPa [14,23], which is significantly higher than the experimental measurements. The magnetic properties of manganese borides are equally complex. The experimental reproducibility is always as low as the transition temperatures and magnetic properties in MnB_2 [24–27]. Additionally, others such as the spin-glass behavior in Mn_2B [12] and significant variations in magnetic moments at different sites of Mn_3B_4 [28], are also noteworthy.

*Contact author: baokuo@jlu.edu.cn
†Contact author: cuitian@nbu.edu.cn

These disputes arise, on one hand, from experimental challenges such as difficulties in controlling the high-temperature phase diagrams of borides and the quality of synthesized samples. On the other hand, most theoretical predictions start from the generalized-gradient approximation (GGA) level, but considering the complex magnetism of Mn, it is crucial to include magnetic considerations and functional corrections to have better potential-energy surfaces of the Mn-B system. The $+U$ method is commonly employed to compensate the underestimation of exchange-correlation energy caused by magnetism [29]. However, choosing an appropriate U value to the match experimental outcomes could be tricky and sometimes unnecessary for magnetic compounds [9,19,22]. Therefore, we note that the Meta-GGA strongly constrained and appropriately normed (SCAN) functional could be more effective at capturing the physics of strongly correlated materials, despite often overestimating magnetic moments [30]. Additionally, a neural network functional trained on the SCAN functional, termed the physically constrained neural network (pcNN) functional, has shown enhanced predictive capabilities under more constraints [31]. This could potentially provide a more direct and effective description of the Mn-B system. Therefore, we hereby explore overlooked correlation effects with pcNN functional within the Mn-B system, and give clues for the inaccurate predictions caused by the overlooked correlation effects. And, the relevant tests will also be discussed.

In this context, we aim to comprehensively understand the rich phenomena exhibited by manganese borides. First, to establish stable structures is crucial for subsequent property analysis. Therefore, we reevaluate their convex hull to ensure the accuracy of the structural characterization. Subsequently, we compare the simulated results with the experimental data, and address the existing controversies. Then, we delve into the mechanical properties of manganese borides. By constructing descriptors based on the overall bond strength of their unit cells, we try to establish a connection between these descriptors and hardness to give a robust description of their mechanical behavior. Crucially, we expand our investigation to explore the intricate magnetism of manganese borides. Leveraging electronic structure calculations and spin dynamics results, we contrast our findings with the experimental data to distinguish their applicability on the local-moment model. Furthermore, we conduct a detailed discussion on the magnetic phenomena of this system. We hope that our research provides valuable insights into the mechanical and magnetic properties of intermetallic compounds, and aid in the investigation of magnetic phenomena in materials science.

II. METHODS

In this work, we performed the structural relaxation and property simulations within a density-functional theory framework and the projector augmented-wave method [32] as implemented in the Vienna *Ab initio* Simulation Package, VASP [33], and allowed spin polarization due to the magnetic nature of manganese-containing materials. The pcNN exchange-correlation functional was adopted [31]. The pcNN functional provides a stable description for various magnetic materials that is quite close to experimental results, though it slightly overestimates some experimental magnetic moments. We select several magnetic materials to test and compare the PBE, SCAN, and pcNN functionals, and include the results and discussion in the Supplemental Material [34] (see also Refs. [8–14,22,23,30,31,35–55] therein). The valence states considered in this paper are $3p^6\ 3d^6\ 4s^1$, $2s^2\,2p^1$ for Mn and B atoms, respectively. The plane-wave cutoff energy is 600 eV throughout this study. We use a second-order Methfessel-Paxton [56] electron smearing with $\sigma = 0.2$ eV. The convergence criterion on forces is 0.01 eV/Å and the energy tolerance is 10^{-8} eV. The bulk structures are fully optimized for all the degrees of freedom. The samplings of the Brillouin zone are obtained from a Gamma-centered k-mesh spacing of $2\pi \times 0.03$ Å^{-1} in the calculations. The crystal orbital Hamilton population (COHP) [57] is calculated using the LOBSTER package to analyze the bonding properties. The calculation of magnetic exchange parameters is conducted using the TB2J package with the magnetic force theorem based on the Heisenberg model [58]. Localized wave functions are obtained through the WANNIER90 package [59]. The final spin dynamics calculations are conducted using the Landau-Lifshitz-Gilbert equation, employing a $20 \times 20 \times 20$ supercell, and performed with the VAMPIRE software [60].

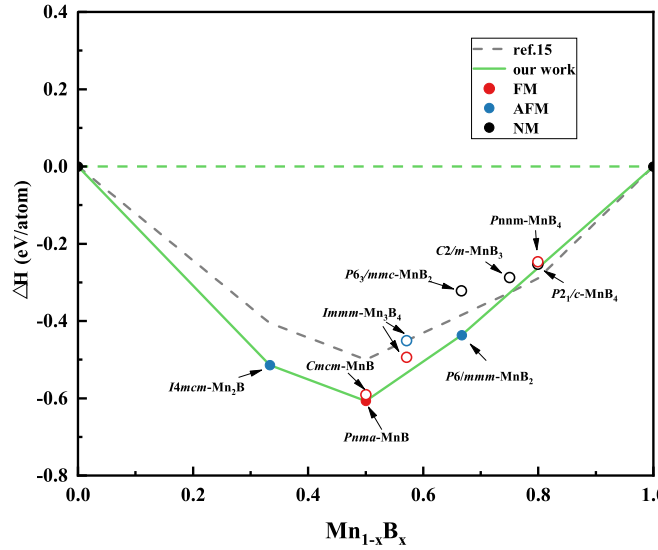

FIG. 1. The convex hull of $Mn_{1-x}B_x$. We use the results from Niu *et al.* [15] for comparison. Considering the influence of collinear magnetism and correlations, we have reevaluated the system. In the representation, ferromagnetic states are denoted in red, antiferromagnetic states in blue, and nonmagnetic states in black. Solid symbols represent stable phases that fall within the convex hull, while hollow symbols represent metastable phases that do not lie on it.

III. RESULTS AND DISCUSSION

A. Convex hull

We optimized the manganese-boride systems with the pcNN functional and recalculated their convex hulls, considering their collinear magnetism. Figure 1 shows that the density-functional theory (DFT) formation enthalpies of the $Mn_{1-x}B_x$ structures. The convex hull, connecting

nonmagnetic (NM)-α-Mn(tI58), antiferromagnetic (AFM)-Mn_2B (oI12), ferromagnetic (FM(-MnB (oP8), AFM-MnB_2 (hP3), and NM-α-B (hR12), is drawn for the most stable ground-state phase. Then, other key observations can be summarized as follows.

1. α-Mn

Manganese is one of the most complex metallic elements that assume many different stable crystal phases. We will focus solely on the magnetic properties of room-temperature phase α-Mn (space group I-43m) to have certain understanding of it, as it consists of quite many atoms (58 atoms) and is a "self-intermetallic" compound. In experiments, α-Mn exhibits antiferromagnetic behavior with a Néel temperature of 95 K, and it shows lattice distortion at low temperatures [61]. Early studies showed that even when considering spin polarization, the results obtained from local-density approximation–GGA simulations only converged to collinear magnetic states and still had significant discrepancies with experimental data [62]. Recently, simulations of the magnetic properties of α-Mn revealed that by incorporating spin-orbit coupling and employing the SCAN functional, the system converges to a noncollinear antiferromagnetic state [63]. Therefore, manganese itself is highly intricate. Here, for convenience, we exclusively treated α-Mn as a nonmagnetic state in our study.

2. Mn_2B

In the early studies, Simsek *et al.* [64] reported the ferromagnetic behavior of Mn_2B at 300 K, while Ma *et al.* [12] reported it to exhibit spin-glass behavior with a Néel temperature of 43 K. Meanwhile, Mohn [65] reported the nonmagnetic nature of Mn_2B through calculations, and this result is consistent with what we predicted using the Perdew-Burke-Ernzerhof (PBE) functional. Our results indicate a slight deviation from the experimentally observed Al_2Cu-type tI12-Mn_2B structure [12,66,67]. When considering an antiferromagnetic configuration along the crystallographic a- and b axes, it was observed that the presence of magnetostriction induced a change in symmetry, leading to the identification of a structure known as oI12 (space group: *Ibma*). Additionally, it would converge to a nonmagnetic state along the c axis, possibly due to the presence of anisotropy, and the lattice c is also overestimated compared with the experiments as shown in Table I. The specific configuration can be seen in Fig. S1 of Supplemental Material [34]. It is worth noting that the two magnetic phases, AFM-a and AFM-b oI12-Mn_2B, are almost degenerate in terms of enthalpy, with AFM-b oI12-Mn_2B having slightly lower enthalpy [$\Delta E \sim 9$ meV/f.u. (formula units)], and lattice contraction occurring in the directions where antiferromagnetic ordering is present. These two magnetic structures are equivalent, highlighting a key characteristic of Mn_2B's magnetic structure: the presence of multiple equivalent spin alignment directions. Coupled with the competitive positive and negative exchange interactions observed over short distances, as shown in Fig. S3 of the Supplemental Material [34], this characteristic may lead to the coexistence and competition between ferromagnetic and antiferromagnetic coupling. The complexity of these microscopic magnetic interactions offers a solid theoretical basis for explaining the spin glass behavior observed in polycrystalline Mn_2B samples during experiments [12]. Furthermore, we can also compare the same structure of Fe_2B, which reveals an interesting observation: Fe_2B is a strong ferromagnet with a *Curie* temperature (T_C) of 1017 K [68], whereas Mn_2B exhibits a very low transition temperature. The main difference between them lies in the fact that in Fe_2B, the shortest Fe–Fe bond length is 2.41 Å, while in Mn_2B, it is 2.29 Å. This shorter bond length could enhance exchange interactions, but excessively strong interactions could also repel the originally localized 3d electrons, forcing them to become itinerant within the lattice. As a result, complex exchange interactions occur in Mn_2B, leading to its spin frustration. It is also worth mentioning that the previously predicted Mg_2Cu-type Mn_2B [15] (space group: *Fddd*) does not exist within our framework described, as it is thermodynamically unstable.

3. MnB

MnB exhibits two phases: oC8-MnB and oP8-MnB. These two phases are very close in terms of enthalpy, as shown in Fig. 1 or Table I. Both phases are ferromagnetic and are the only experimentally obtained ferromagnetic phases in the manganese borides. According to *Klemenz et al.*'s work, the oC8-MnB can further transform into oP8-MnB at temperatures above 1523 K [69]. Our simulation using the pcNN functional for oP8-MnB yielded a magnetic moment of 2.3 μB/Mn, slightly higher than the experimental measurement of 1.9 μB/Mn [9,70]. Furthermore, previously synthesized oC8-MnB samples were found to contain defects [13,69]. However, in a recent development, Kalyon *et al.* successfully synthesized a pure phase of oC8-MnB [71], with a measured magnetic moment of 1.54 μB/Mn. This value is lower than our simulated value of 2.3 μB/Mn. Additionally, the pure oC8-MnB is reported to have a Curie temperature (T_C) of 456 K, and the material exhibits spin-canted magnetism along the crystallographic c axis. Meanwhile, Bocarsly *et al.* also pointed out that MnB, with strongly coupled magnetic and structural transitions, exhibits excellent magnetocaloric properties [72].

4. Mn_3B_4

Mn_3B_4 exhibits layered structures. However, unlike MnB_2, where Mn and B atoms form independent layers, in Mn_3B_4, Mn and B atoms are mixed in a single layer, as shown in Fig. 2. Experimental evidence suggests its antiferromagnetism. Moreover, Mn_3B_4 is the only phase in our results that deviates from experimental observations. It is worth noting that in our simulation results, although the enthalpy of the ferromagnetic state is lower, it still does not fall within the convex hull. Therefore, for a better comparison, we continue to use the antiferromagnetic state corresponding to the experimental results for the subsequent discussion. The simulated magnetic moments are 2.84 μB/Mn for Mn(2a) and 2.61 μB/Mn for Mn(4j), while experimental measurements yield 2.92 μB/Mn for Mn(2a) and 0.44 μB/Mn for Mn(4j) [28]. Additionally, as shown in Fig. 2(c), the local coordination environment for Mn(2a) atoms in oI14-Mn_3B_4 is identical to that of Mn atoms in hp3-MnB_2, and Mn(4j) atoms in oI14-Mn_3B_4 mirror the coordination environment of Mn

TABLE I. DFT formation enthalpies (ΔH in eV per atom), optimized lattice parameters (Å), and corresponding experimentally obtained lattice parameters (Å) for the manganese borides.

Phase	Ordering	Space-group cell (calc.)	Pearson symbol	Space-group cell (exp.)	ΔH
Mn_2B	*AFM*-[010]	*Ibam* $a = 5.189$ $b = 5.065$ $c = 4.274$	*oI*12	*I4/mcm*[a] a = b = 5.122 c = 4.188	−0.468
MnB	*FM*	*Pnma* $a = 5.488$ $b = 2.953$ $c = 4.108$	*oP*8	*Pnma*[b] a = 5.637, b = 2.994 c = 4.180	−0.608
MnB	*FM*	*Cmcm* $a = 2.982$ $b = 7.627$ $c = 2.935$	*oC*8	*Cmcm*[c] $a = 3.009$ $b = 7.639$ $c = 2.946$	−0.593
Mn_3B_4	*AFM*	*Immm* $a = 2.941$ $b = 3.093$ $c = 12.787$	*oI*14	*Immm*[d] $a = 2.963$ $b = 3.038$ $c = 12.844$	−0.450
MnB_2	*AFM*	*P6/mmm* $a = b = 3.005$ $c = 3.038$	*hP*3	*P6/mmm*[e] $a = b = 3.010$ $c = 3.040$	−0.439
MnB_2	*NM*	$P6_3/mmc$ $a = b = 2.778$ $c = 6.953$	*hP*6		−0.323
MnB_3	*NM*	*C2/m* $a = 7.078$ $b = 2.836$ $c = 5.868$ $\beta = 90.624°$	*mC*16		−0.288
MnB_4	*NM*	$P2_1/c$ $a = 5.429$ $b = 5.312$ $c = 5.463$ $\beta = 114.757°$	*mP*20	$P2_1/c$ [f] $a = 5.476$ $b = 5.367$ $c = 5.502$ $\beta = 115.04°$	−0.254
MnB_4	*FM*	*Pnnm* $a = 4.604$ $b = 5.316$ $c = 2.941$	*oP*10	$P2_1/n$ [f] $a = 4.630$ $b = 5.365$ $c = 2.948$ $\beta = 90.31°$	−0.246

[a]Reference [12]; [b]Reference [9]; [c]Reference [71]; [d]Reference [11]; [e]Reference [8]; [f]Reference [22].

atoms in *oC*8-MnB. The mixing of these local environments seems to suggest that Mn_3B_4 might be a metastable phase composed of two mixed phases. What adds more intrigue is the observation of spin-tilting phenomena in both MnB_2 and Mn_3B_4 at low temperatures, with MnB_2 at 130 ∼ 157 K [24,26] and Mn_3B_4 observed at 226 K [73]. This raises curiosity about whether a small portion of MnB_2 plays a role in influencing the properties of Mn_3B_4. Further investigations are necessary to determine if other factors, such as defects, contribute to the significant difference in magnetic moments observed at different Wyckoff sites in Mn_3B_4.

5. MnB_2

MnB_2 has been the subject of controversy, as the predicted ReB_2-type structure (space group: $P6_3/mmc$) [15], which could be the most stable phase for MnB_2 without magnetism. However, it is found to be thermodynamically unstable in our results, as shown in Fig. 1. The antiferromagnetic

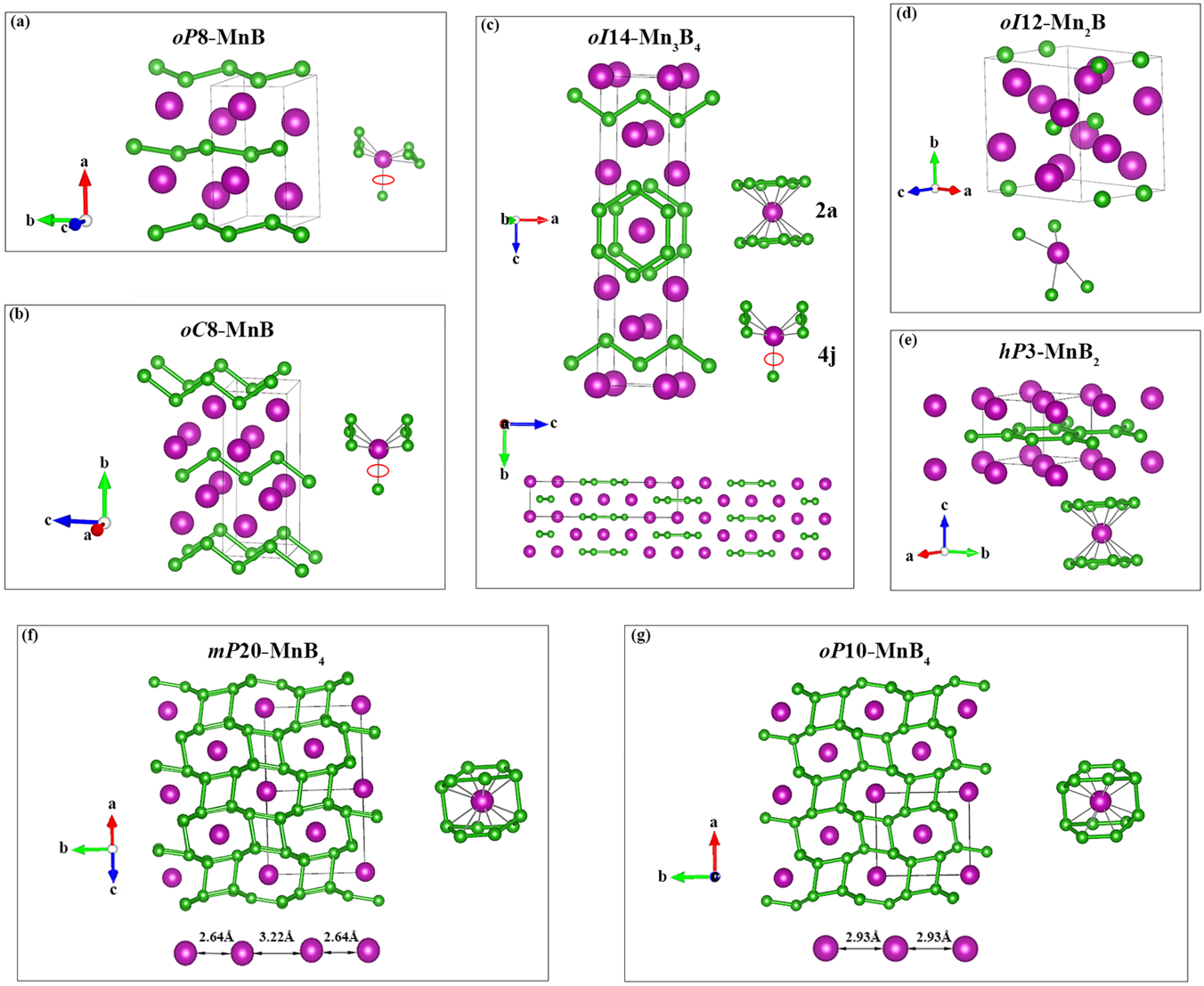

FIG. 2. The structures of manganese borides are depicted as follows: (a) *oP*8-MnB, (b) *oC*8-MnB, (c) *oI*14-Mn_3B_4, (d) *oI*12-Mn_2B, (e) *hP*3-MnB_2, (f) *mP*20-MnB_4, and (g) *oP*10-MnB_4. In these structures, boron forms chains, layers, and cages, while also showcasing the local coordination environments of manganese.

MnB_2 with the AlB_2-type structure, belonging to the space group *P6/mmm*, falls within the convex hull. One possible reason for this is the insufficient consideration of correlations previously. Moreover, in this AlB_2-type layered structure, the interlayer dispersion forces are equally crucial and need to be considered [74]. However, these considerations could also be applicable to the pcNN functional we are using. MnB_2, the simplest structure among manganese borides, and adopts a hexagonal layered structure with Mn atoms sandwiched between two hexagonal rings. The calculated local magnetic moment in this phase is 3.10 μB/Mn, which is a little higher than the value of 2.76 μB/Mn obtained in Regnat's paper [26]. Additionally, it has a significantly high Néel transition temperature (T_N) of around 1130 K. What is more interesting is its manifestation of canted antiferromagnetism at approximately 130 K, resulting in a net ferromagnetic moment. This phenomenon sheds light on the previous misconception of considering it as ferromagnetic [27,75]. The phenomenon of spin canting becomes more pronounced on one hand due to the itinerant characteristics of magnetic moments at low temperatures. On the other hand, it might be attributed to the presence of anisotropy such as the Dzyaloshinskii-Moriya interaction, which warrants further investigation.

6. MnB_4

*mP*20-MnB_4 exhibits *Peierls* distortions and represents a nonmagnetic phase, while *oP*10-MnB_4 shows weak ferromagnetic local magnetic moment (0.74 μB/Mn). In MnB_4, as depicted in Figs. 2(f) and 2(g), the two phases appear somewhat similar, but they diverge in forming a one-dimensional manganese chain perpendicular to the viewing direction. In the *mP*20-MnB_4, Mn atoms undergo dimerization, while in the *oP*10-MnB_4, a uniform manganese chain is formed. These two phases are energetically close to each other, and it is possible to transform from *mP*20-MnB_4 to *oP*10-MnB_4 by

heating to about 650 K [76]. It is worth noting that while both phases of MnB_4 are not strictly on the convex hull, its proximity suggests it can be easily achieved by controlling specific experimental conditions, such as high-temperature and high-pressure conditions [10,22,77]. The main controversy regarding MnB_4 lies in its ground-state or magnetic properties. Experimental measurements reveal a significant sample dependence in synthesized MnB_4 samples, indicating the potential for MnB_4 to be a diamagnetic semiconductor [78]. Additionally, Knappschneider *et al.* [76] discovered a transition in MnB_4 from a low-temperature *p*-type semiconductor to a high-temperature *n*-type metal. This transition was also previously predicted in another study [79], and although we did not explicitly consider the impact of temperature, valuable insights could still be gleaned by examining the close energies of both phases.

In short, we reevaluated the convex hull and optimized lattice parameters, obtaining values close to experimental ones. According to our simulation results, the complexity observed in manganese borides could be attributed to challenges in accurately determining and analyzing the stable structures of the two phases due to their closely related energies. For example, in MnB and MnB_4, the more stable structures often exhibit higher complexity, while at elevated temperatures, the structurally more ordered phases become more accessible [69,76]. Although this explanation holds, controlling experimental phase diagrams is quite challenging. In contrast, theoretical simulations present a distinct advantage: our simulations could have the potential to provide insights into comprehending the magnetic behavior and electronic properties of manganese borides. Furthermore, if not specified in the subsequent sections, the consideration of magnetism aligns with the information presented in Table I.

B. Bonding properties

The mechanical properties of transition-metal borides have long been a subject of interest and scrutiny [80,81], as boron can form rich covalent networks within them. Additionally, manganese borides possess magnetic characteristics, adding an intriguing dimension to the correlation between their bonding properties. In this context, we computed the integrated COHP (iCOHP), a method intuitively assessing bonding strength in solid-state materials, to analyze the bonding properties of the experimentally synthesized manganese borides under consideration. The relevant results are listed in Table II. Negative values of iCOHP serve as indicators of bonding strength in our assessment. The shorter bond lengths usually imply a higher bond strength, but the actual strength is also influenced by the coordination environment. For instances like *oP*8-MnB, *oC*8-MnB, and *oI*14-Mn_3B_4, despite their relatively long Mn–B bond lengths highlighted in bold in Table II, high bond strength is observed. This phenomenon is notably associated with the Mn–B bonds marked by red circles in Fig. 2. Clearly, these Mn–B bonds exhibit a distinct feature where the Mn–B bond exclusively shares the electron density in approximately half of the region surrounding the Mn atoms, resulting in elevated electron density within the bonding region, which is responsible for their high bond strength. Moreover, by examining the bond-length distributions as shown in Table II, it is evident that *oC*8-MnB exhibits a higher degree of structural order compared to *oP*8-MnB. Similarly, *oP*10-MnB_4 displays a more ordered structure compared to *mP*20-MnB_4.

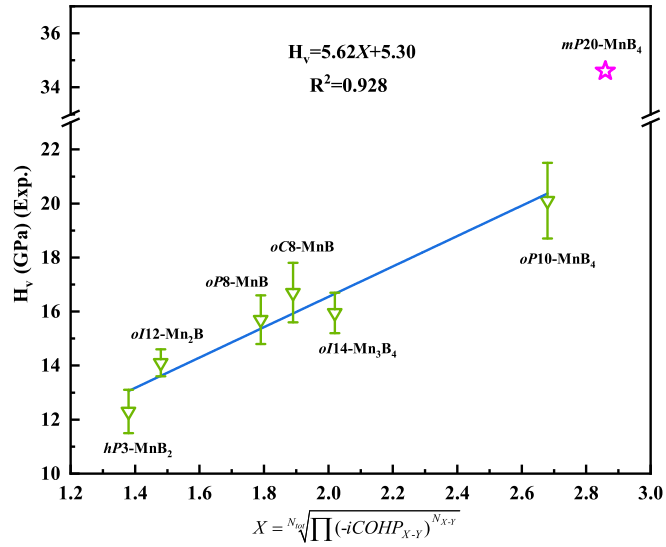

FIG. 3. Descriptors reflecting the binding properties of the constructed system in response to its relationship with Vickers hardness from the experiment. The magenta pentagrams represent the outlier experimental values obtained from the *mP*20-MnB_4 [22], while the other green triangles represent the measured values of other manganese borides from other experiments, which can be found in Table II.

Hardness is a parameter that can intuitively reflect the mechanical properties of materials, and it largely depends on plastic deformation, which is closely associated with the generation and mobility of dislocations [82]. The process of plastically shearing such a crystal involves the breaking and reforming of electron-pair bonds. Therefore, if we assess the overall bond strength of compounds, we can also obtain a good estimate of their hardness. As we have already employed −iCOHP to quantify the bonding strength in manganese borides, we directly utilized their geometric mean to construct a descriptor, $\sqrt[N_{tot}]{\prod(-iCOHP_{X-Y})^{N_{X-Y}}}$, measuring the overall bonding strength of the unit cell. The $-\text{iCOHP}_{X-Y}$ represents the negative value of the integrated COHP of the *X*–*Y* bond, while the N_{X-Y} represents the number of *X*–*Y* bonds per formula unit within a unit cell. N_{tot} represents the total number of *X*–*Y* bonds per formula unit within a unit cell that needs to be considered. This means that not all bonds would be included in the consideration, with the primary focus on Mn–B bonds and B–B bonds, whose number and bond length are listed in Table II. The contribution of Mn–Mn bonds could be disregarded due to their relatively weaker bonding. However, in the case of *oI*12-Mn_2B, a robust Mn–Mn bond strength is evident, comparable even to its Mn–B bonds. Therefore, we extended our consideration to include the next-nearest neighbor Mn–Mn bond with a length of 2.51 Å in *oI*12-Mn_2B. With the considerations mentioned above, the results are presented in Fig. 3. It is pleasantly surprising to observe an approximately linear relationship. However, the previously measured hardness of 34.6 GPa for *mP*20-MnB_4 might appear

TABLE II. The distribution of Mn-B, B-B, and Mn-Mn bond lengths in manganese borides has been examined. We analyzed the distributions of bond lengths, with the number of each bond averaged per formula unit within a unit cell provided in square brackets. Concurrently, we assessed their negative iCOHP and constructed descriptors reflecting the bonding properties of the manganese borides and experimentally measured Vickers hardness values.

Phase	$d_{\text{Mn-B}}$ [$N_{\text{Mn-B}}$/f.u.]	−iCOHP (Mn–B)	$d_{\text{B-B}}$ [$N_{\text{B-B}}$/f.u.]	−iCOHP (B–B)	$d_{\text{Mn-Mn}}$ [$N_{\text{Mn-Mn}}$/f.u.]	−iCOHP (Mn–Mn)	$\sqrt[N_{\text{tot}}]{\prod(-iCOHP_{X-Y})^{N_{X-Y}}}$	H_v (exp)
AFM-[010]-*oI*12-Mn_2B	2.20 [8]	1.83	2.13 [0.5]	3.50	2.29 [1]	1.60	1.48	14.1[a]
					2.51 [2]	0.51		
FM-*oP*8-MnB	2.16 [2]	1.90	1.79 [0.5]	6.01	2.62 [0.5]	0.52	1.79	15.7[b]
	2.18 [3]	1.45						
	2.20 [1]	1.37						
	2.23 [1]	**2.20**						
FM-*oC*8-MnB	2.17 [4]	1.88	1.80 [0.5]	6.00	2.63 [0.5]	0.33	1.89	16.7[c]
	2.19 [1]	**2.24**						
	2.20 [2]	1.33						
AFM−*oI*14-Mn_3B_4	2.15 [4]	1.45	1.73 [1]	7.57	2.77 [4]	0.24	2.02	16.3[d]
	2.20 [8]	1.75	1.76 [4]	6.88				
	2.22 [2]	**2.48**						
	2.30 [8]	1.21						
AFM-*hP*3-MnB_2	2.30 [12]	1.04	1.73 [2]	7.64	3.01 [3]	0.11	1.38	12.1[e]
NM-*mP*20-MnB_4	1.99 [1]	2.37	1.68 [1]	7.84	2.64 [0.5]	0.42	2.86	34.6[f]
	2.02 [1]	2.21	1.72 [1]	7.15	3.22 [0.5]	0.05		
	2.07 [1]	2.12	1.81 [1]	6.27				
	2.08 [1]	2.04	1.82 [1]	6.05				
	2.10 [1]	1.78	1.84 [1]	5.96				
	2.12 [1]	1.66	1.86 [1]	4.70				
	2.16 [1]	1.62	1.90 [1]	4.19				
	2.18 [1]	1.55	2.10 [1]	2.27				
	2.20 [1]	1.51						
	2.23 [1]	1.40						
	2.26 [1]	1.24						
	2.29 [1]	1.12						
FM-*oP*10-MnB_4	2.00 [2]	2.27	1.70 [2]	7.40	2.94 [1]	0.17	2.68	20.1[g]
	2.10 [2]	1.74	1.82 [4]	6.15				
	2.14 [4]	1.78	1.88 [1]	4.44				
	2.23 [4]	1.34	2.11 [1]	2.22				

[a]Reference [12]; [b]Reference [9]; [c]Reference [13]; [d]Reference [11]; [e]Reference [8]; [f]Reference [22].; [g]Reference [10].

as an outlier [22]. Nevertheless, upon closer examination, Figs. 1 and 2 reveal that the energy and structural differences between *mP*20-MnB_4 and *oP*10-MnB_4 are minimal, suggesting that their mechanical properties should not be diverged significantly. Based on our descriptors, they are also similar. Therefore, the hardness of *mP*20-MnB_4 seems to be significantly overestimated. According to our estimation, its H_v is approximately 21.3 GPa. Similar controversies have arisen previously in the isostructural FeB_4, where experimental measurements initially indicated its classification as a superhard material [39], but subsequent theoretical studies refuted this claim [83,84]. Based on our results, assessing the strength of bonds offers a straightforward method for evaluating the hardness of the system. The most evident example is MnB_2, which as a layered material exhibits the lowest hardness, a characteristic that is fully captured in our results. We believe this approach could provide a simpler perspective for understanding the mechanical properties of materials and streamline the prediction process. We also employed descriptors calculated using the PBE functional and used Guo's hardness model [51] to calculate the hardness of the Mn-B system and compared it with experimental results. The relevant discussion and details have been included in the Supplemental Material [34].

C. Magnetism and electronic structures

The magnetic properties and electronic structure of manganese borides are also interesting to us. The density of states (DOS) plots for these manganese borides are presented in Fig. 4. Except for NM−*mP*20-MnB_4 and AFM−*hP*3-MnB_2, which have a density of states at the Fermi level [$N(E_F)$] that is nearly zero, the other materials exhibit nonzero $N(E_F)$, indicating that they are metallic. Typically, the 3*d* and 4*s* electrons of transition metals can be considered to be freely itinerant within the lattice [85,86]. However, according to our results, the 4*s* electrons of all manganese borides contribute almost nothing to the E_F, and the primary contribution comes from the Mn-3*d* electrons. This means that when the 3*d* electrons form localized magnetic moments,

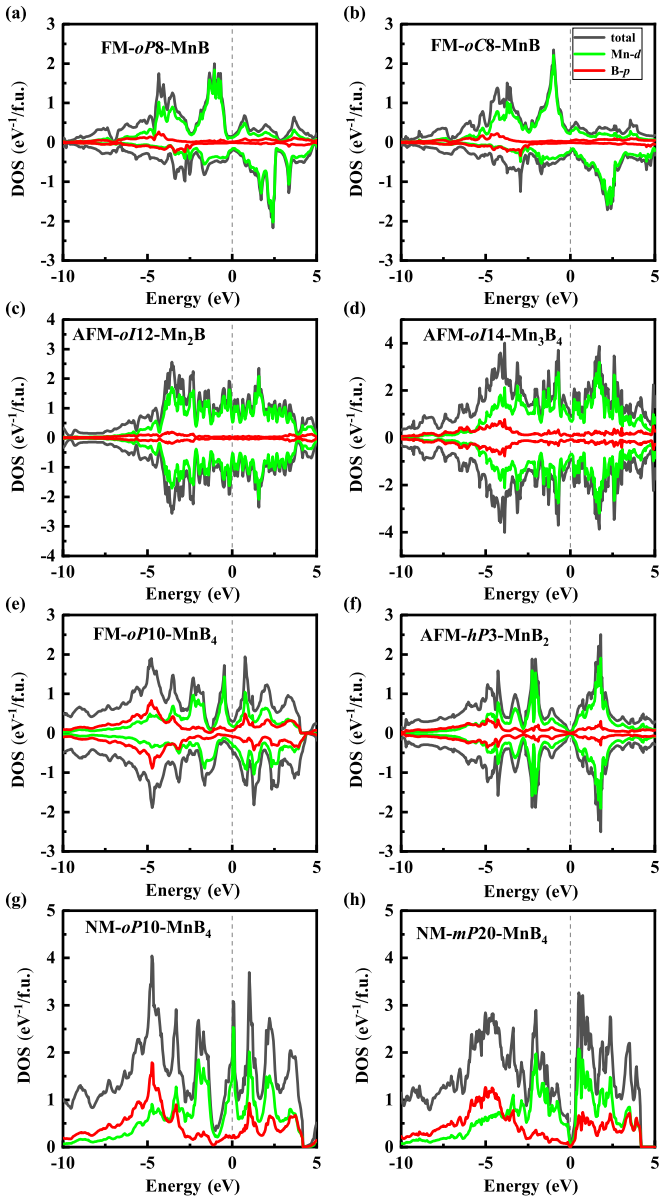

FIG. 4. The total and partial density of states of manganese borides are as follows: (a) FM-*oP*8-MnB, (b) FM-*oC*8-MnB, (c) AFM-*oI*14-Mn_3B_4, (d) AFM-*oI*12-Mn_2B, (e) AFM-*hP*3-MnB_2, (f) NM-*mP*20-MnB_4, and (g) NM-*oP*10-MnB_4.

they also exhibit itinerant characteristics, which lead to fractional magnetic moments. The local-moment picture and the itinerant electron scenario have historically served as explanatory frameworks for understanding magnetic properties in condensed matter. In reality, real metals exhibit a mix of characteristics from both, blending local-moment and itinerant magnetism. This tendency varies among different manganese borides. AFM−*hP*3-MnB_2 exhibits the minimum $N(E_F)$ among all magnetic manganese borides, almost approaching zero, indicating that relative to other manganese borides, its 3*d* electrons are more localized. Additionally, its simulated magnetic moment is close to an integer value of approximately 3 μB. Such observations are consistent with findings from Regnat [26], suggesting that AFM-*hP*3-MnB_2 is a local moment antiferromagnet. Then, in Fig. 4(g), we

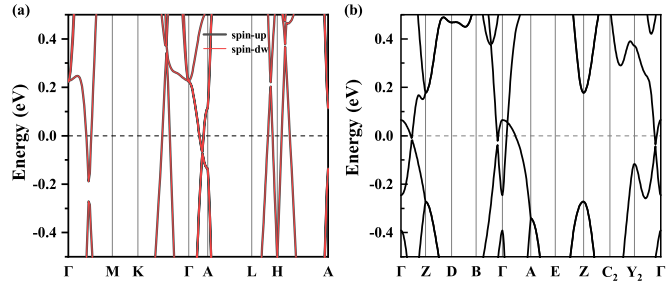

FIG. 5. The band structures of (a) AFM-*hP*3-MnB_2 and (b) NM-*mP*20-MnB_4 are shown; they do not exhibit distinct band crossings near the E_F and are more reminiscent of a trivial semimetal.

illustrate the DOS for NM-*oP*10-MnB_4. Due to the strong localized nature of its 3*d* electrons, a peak is evident in its $N(E_F)$, which is detrimental to the system's stability. On the one hand, according to the *Stoner mechanism*, the system tends to undergo spin polarization, forming magnetic moments to enhance stability, and its significant $N(E_F)$ also indicates its good metallic properties, as shown in Fig. 4(e). On the other hand, this instability is also associated with the one-dimensional manganese chains. According to the Peierls mechanism, manganese chains might undergo dimerization, leading to a reduction of the $N(E_F)$ and the formation of a pseudogap. Thus, the experimental observation of a transition from a low-temperature *p*-type semiconductor to a high-temperature *n*-type metal [76] could be clearly explained by the DOS profiles of *mP*20-MnB_4 and *oP*10-MnB_4, as illustrated in Fig. 4. Furthermore, it is noteworthy that both AFM-*hP*3-MnB_2 and NM-*mP*20-MnB_4 exhibit pseudogap features near the E_F. This piqued our interest in their band structures, and the relevant results are presented in Fig. 5. We anticipate these materials to exhibit features of a Dirac cone near the E_F, which might involve certain topological properties. However, upon a detailed examination within the range of $E_F \pm 0.5$ eV, we find that they do not display band crossings near the E_F in their band structures. Therefore, they might not possess well-defined topological properties but rather resemble characteristics closer to semimetals.

We also calculated the magnetic transition temperatures of these manganese borides, and their comparison with experimental results is presented in Table III. The band structures

TABLE III. Through spin dynamics calculations, we simulated the Curie temperature (T_C)–Néel temperature (T_N) and compared it with experimentally measured T_C/T_N values.

Phase	T_C/T_N (exp.)	T_C/T_N (calc.)
*AFM-b-oI*12-Mn_2B	43[a]	784
*FM-oP*8-MnB	546[b], 566[c], 574[d]	641
*FM-oC*8-MnB	466[d],545[e]	632
FM-*oI*14-Mn_3B_4	390 and 214[f]	822
AFM-*hP*3-MnB_2	760[g], 885[h], 1130[i]	1180
*FM-oP*10-MnB_4		1.6

[a]Reference [12]; [b]Reference [9]; [c]Reference [88]; [d]Reference [71]; [e]Reference [69]; [f]Reference [11]; [g]Reference [24]; [h]Reference [25]; [i]Reference [26].

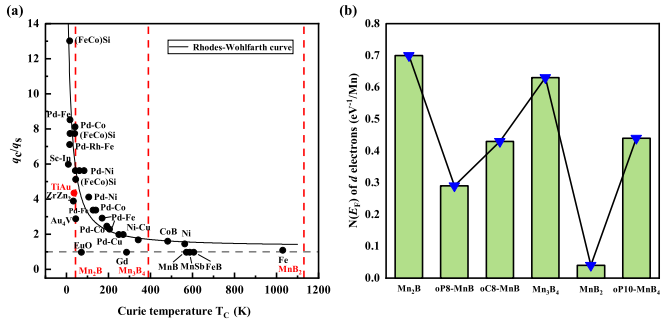

FIG. 6. (a) The Rhodes–Wohlfarth ratio q_c/q_s for various magnetic materials. Reproduced from Ref. [87]. Red indicates its antiferromagnetic behavior, with the corresponding transition temperature being T_N. For MnB, the q_c data are available, whereas for other magnetic manganese borides, such data are currently unavailable. Only the transition temperatures are measured, hence represented by dashed lines. This allows for an estimation of their q_c/q_s. (b) The density of states of d electrons at the Fermi level for magnetic manganese borides.

fitted with localized Wannier functions and the computed exchange-interaction parameters are presented in Figs. S2 and S3 of Supplemental Material [34]. (The calculation of its exchange parameters (J) follows the conventions of the Heisenberg model selected in TB2J [58]). The cutoff distance for exchange interactions considered in spin dynamics calculations is set at 3.5 Å, as illustrated in detail in Fig. S3 of Supplemental Material [34]. The results of the spin dynamics simulations are presented in Fig. S4 of the Supplemental Material [34]. However, there are still some discrepancies when comparing the obtained magnetic transition temperatures with experimental values. This is primarily due to the fitting of J based on the local-moment Heisenberg model and the rigid spin rotation assumption [58]. When the spins tend towards delocalization, the results tend to become invalid. The localization of magnetic moments for intermetallic compounds could be quantitatively determined by the Rhodes-Wohlfarth ratio q_c/q_s [89]. Here, q_c represents the magnetic carriers in the paramagnetic state at high temperatures, and the number of carriers q_c can be experimentally obtained from a linear fit of $1/\chi(T)$. On the other hand, q_s represents the magnetic carriers in the ordered state at low temperatures, which can be obtained from the saturation magnetization at low temperatures under strong magnetic fields [87]. For local-moment systems q_c/q_s should equal unity, while for itinerant moment systems $q_c/q_s \gg 1$, with the latter also tending to low magnetic transition temperatures [87]. From Fig. 6(a), reproduced from Ref. [87], we could observe that based on the measured data, the ratio q_c/q_s for MnB is close to 1, indicating that its magnetic moment tends to be more local. However, for other manganese borides, there are insufficient $\chi(T)$ data to fit q_c, making it challenging to assess the specific localization of magnetic moment. Nonetheless, according to the Rhodes-Wohlfarth curve in Fig. 6(a), we can see that MnB_2, with its extremely high Néel temperature ($T_N \sim 1130$ K) [26], is practically approaching the local limit, which aligns with our understanding of it as a local-moment antiferromagnet. According to our simulation results, the transition temperatures of MnB_2 and MnB align with experimental findings, although the transition temperature of MnB is slightly overestimated by 100 K, which might also be attributed to its overestimated magnetic moment. Compared to the complex magnetism of other manganese borides, this overestimation for MnB still could be considered acceptable. Hence, the Rhodes-Wohlfarth curve seems to provide a criterion to assess whether a system can be described by a local-moment Heisenberg model. Mn_2B, with a T_N of only 43 K, is approaching the itinerant limit according to the Rhodes-Wohlfarth curve. Experimentally, it is also identified as a spin-frustrated spin glass [12], indicating the presence of complex interactions between itinerant magnetic moments. This kind of magnetic frustration system is beyond the scope of our study, and might not be adequately described by a local-moment model. Higher-order interactions or interactions between spin and other degrees of freedom might need to be considered. Simultaneously, it can be observed from Fig. 6(b) that there is a significant $N(E_F)$ contributed by $3d$ electrons. For the discrepancies in the simulation of Mn_3B_4, on the one hand, it was previously suggested that it might represent a mixed metastable phase. On the other hand, even when considering its antiferromagnetic configuration, the simulated exchange interaction still tends to favor ferromagnetism, as depicted in Fig. S3 of Supplemental Material [34]. This finding aligns with our assessment of its ferromagnetic ground state. Additionally, from Fig. 6(b), its significant $N(E_F)$ suggests that its magnetic moment might lean towards itinerant characteristics. These observations indicate a potential explanation for the discrepancy between simulation results and experiments. Therefore, further experimental measurements are required to reassess their properties. Finally, in the case of $oP10$-MnB_4, although Mn atoms exhibit weak magnetic moments, they form isolated one-dimensional magnetic chains. The distance between these chains is approximately 3.8 Å, significantly spaced within the three-dimensional lattice. Therefore, in adherence to the Mermin-Wagner theorem [90], it becomes apparent that long-range magnetic order is unattainable in an isotropic one-dimensional system, aligning closely with our simulation results, where the T_C is nearly zero. Nevertheless, the system might still exhibit significant short-range magnetic correlations and local magnetic moments at low temperatures. This characteristic might explain the observations in related experiments [22].

In summary, based on the $N(E_F)$ and the Rhodes-Wohlfarth curve, we assessed the magnetism of the manganese-boride system. This led to a better understanding of its magnetic properties. When the d electrons of magnetic atoms still exhibited significant $N(E_F)$ after considering spin polarization, it indicated a more itinerant character, suggesting that their exchange interactions might be more complex and could not be simply described by the local-moment Heisenberg model; similarly, the spin dynamics based on it would not apply to such systems. More diverse forms of exchange interactions need to be considered to understand their intricate mechanisms, especially at low temperatures. We hope that our discussion offers some insights into the complex magnetism of intermetallic compounds.

IV. CONCLUSION

We conducted a comprehensive reevaluation of manganese borides by employing the pcNN functional. Our analysis revisits the convex hull to delve into structural controversies, thereby illuminating intriguing phenomena. For instance, the spin glass behavior in Mn_2B may result from the complex interactions caused by the unusually short distances between manganese atoms. Furthermore, the ground state of MnB_2 is identified as its AlB_2-type structure, characterized by a strongly localized antiferromagnetic semimetal. Additionally, we address the debate surrounding the coexistence of two phases in MnB and MnB_4, revealing their close enthalpies. In contrast, Mn_3B_4 is identified as a potentially ferromagnetic and thermodynamically metastable phase, hinting at its capability as a mixed phase of *oC*8-MnB and *hP*3-MnB_2. Our findings also draw a connection between the bonding strength in manganese borides and their observed hardness, offering a better approach for understanding and rapidly estimating the mechanical properties of these systems. Additionally, with our calculated exchange parameters and spin dynamics simulation for magnetic transition temperatures, we observe that MnB_2 and MnB align closely with experimental findings, whereas Mn_2B and Mn_3B_4 exhibit noticeable deviations. The discrepancies in Mn_2B and Mn_3B_4 likely arise from their strong itinerant nature, notably due to the significant DOS of Mn-*d* electrons at the Fermi level. This renders them unsuitable for local-moment models, and analysis using the Rhodes-Wohlfarth curve also suggests their applicability. Furthermore, the presence of magnetic moments in *oP*10-MnB_4, which lacks long-range order due to the substantial distances between the chains, aligns with the Mermin-Wagner theorem. We hope that these findings would illuminate the bonding and magnetic properties of other transition-metal borides and magnetic intermetallic compounds, thus fostering further advancements.

ACKNOWLEDGMENTS

This work was supported by the National Key R&D Program of China (Grants No. 2018YFA0703404 and No. 2017YFA0403704), National Natural Science Foundation of China (Grants No. 11774121 and No. 91745203), and Program for Changjiang Scholars and Innovative Research Team in University. The calculations were performed at Hefei advanced computing center.

[1] Edited by V. I. Matkovich, *Boron and Refractory Borides* (Springer-Verlag, Berlin, 1977), p. 656.

[2] S. Carenco, D. Portehault, C. Boissiere, N. Mezailles, and C. Sanchez, Nanoscaled metal borides and phosphides: Recent developments and perspectives, Chem. Rev. **113**, 7981 (2013).

[3] T. Ma, P. Zhu, and X. Yu, Progress in functional studies of transition metal borides, Chin. Phys. B **30**, 108103 (2021).

[4] S. Kota, M. Sokol, and M. W. Barsoum, A progress report on the MAB phases: Atomically laminated, ternary transition metal borides, Int. Mater. Rev. **65**, 226 (2020).

[5] S. Chakrabarty, A. Thakur, A. Rasyotra, B. Gaykwad, and K. Jasuja, Quasi-two-dimensional nanostructures from AlB_2-type metal borides: Physicochemical insights and emerging trends, J. Phys. Chem. C **127**, 852 (2022).

[6] R. Kiessling, O. Samuelson, G. Lindstedt, and P.-O. Kinell, The borides of manganese, Acta Chem. Scand. **4**, 146 (1950).

[7] I. Binder and B. Post, Manganese diboride, Acta Crystallogr. **13**, 356 (1960).

[8] S. Ma, K. Bao, Q. Tao, C. Xu, X. Feng, P. Zhu, and T. Cui, Investigating robust honeycomb borophenes sandwiching manganese layers in manganese diboride, Inorg. Chem. **55**, 11140 (2016).

[9] S. Ma, K. Bao, Q. Tao, P. Zhu, T. Ma, B. Liu, Y. Liu, and T. Cui, Manganese mono-boride, an inexpensive room temperature ferromagnetic hard material, Sci. Rep. **7**, 43759 (2017).

[10] S. Ma, K. Bao, Q. Tao, Y. Huang, C. Xu, L. Li, X. Feng, X. Zhao, P. Zhu, and T. Cui, Investigation the origin and mechanical properties of unusual rigid diamond-like net analogues in manganese tetraboride, Int. J. Refract. Hard Met. **85**, 104845 (2019).

[11] S. Ma, K. Bao, Q. Tao, C. Xu, X. Feng, X. Zhao, Y. Ge, P. Zhu, and T. Cui, Double-zigzag boron chain-enhanced Vickers hardness and manganese bilayers-induced high d-electron mobility in Mn(3)B(4), Phys. Chem. Chem. Phys. **21**, 2697 (2019).

[12] S. Ma, K. Bao, Q. Tao, Y. Zhao, C. Xu, X. Feng, X. Zhao, Y. Ge, P. Zhu, and T. Cui, Hardness, magnetic, elastic, and electronic properties of manganese semi-boride synthesized by high pressure and high temperature, J. Solid State Chem. **302**, 122386 (2021).

[13] S. Ma, R. Farla, K. Bao, A. Tayal, Y. Zhao, Q. Tao, X. Yang, T. Ma, P. Zhu, and T. Cui, An electrically conductive and ferromagnetic nano-structure manganese mono-boride with high Vickers hardness, Nanoscale **13**, 18570 (2021).

[14] B. Wang, X. Li, Y. X. Wang, and Y. F. Tu, Phase stability and physical properties of manganese borides: A first-principles study, J. Phys. Chem. C **115**, 21429 (2011).

[15] H. Niu, X. Q. Chen, W. Ren, Q. Zhu, A. R. Oganov, D. Li, and Y. Li, Variable-composition structural optimization and experimental verification of MnB_3 and MnB_4, Phys. Chem. Chem. Phys. **16**, 15866 (2014).

[16] C. Xu, K. Bao, S. Ma, Y. Ma, S. Wei, Z. Shao, X. Xiao, X. Feng, and T. Cui, A first-principles investigation of a new hard multi-layered MnB_2 structure, RSC Adv. **7**, 10559 (2017).

[17] X. Yuan, M. Xu, C. Huang, Y. Liang, S. Lin, J. Hao, and Y. Li, Pressure-stabilized MnB_6 that exhibits high-temperature ferromagnetism and high ductility at ambient pressure, J. Mater. Chem. C **10**, 4365 (2022).

[18] S. Aydin and M. Simsek, First-principles calculations of MnB_2, TcB_2, and ReB_2 within the ReB_2-type structure, Phys. Rev. B **80**, 134107 (2009).

[19] H. Gou, G. Steinle-Neumann, E. Bykova, Y. Nakajima, N. Miyajima, Y. Li, S. V. Ovsyannikov, L. S. Dubrovinsky, and N. Dubrovinskaia, Stability of MnB_2 with AlB_2-type structure revealed by first-principles calculations and experiments, Appl. Phys. Lett. **102**, 061906 (2013).

[20] J. Fan, K. Bao, X. Jin, X. Meng, D. Duan, B. Liu, and T. Cui, How to get superhard MnB_2: A first-principles study, J. Mater. Chem. **22**, 17630 (2012).

[21] R. B. Kaner, J. J. Gilman, and S. H. Tolbert, Designing superhard materials, Science **308**, 1268 (2005).

[22] H. Gou, A. A. Tsirlin, E. Bykova, A. M. Abakumov, G. Van Tendeloo, A. Richter, S. V. Ovsyannikov, A. V. Kurnosov, D. M. Trots, Z. Konôpková *et al.*, Peierls distortion, magnetism, and high hardness of manganese tetraboride, Phys. Rev. B **89**, 064108 (2014).

[23] M. Yang, Y. Wang, J. Yao, Z. Li, J. Zhang, L. Wu, H. Li, J. Zhang, and H. Gou, Structural distortion and band gap opening of hard MnB_4 in comparison with CrB_4 and FeB_4, J. Solid State Chem. **213**, 52 (2014).

[24] M. Kasaya and T. Hihara, Magnetic structure of MnB_2, J. Phys. Soc. Jpn. **29**, 336 (1970).

[25] E. Legrand and S. Neov, Neutron diffraction study of MnB_2, Solid State Commun. **10**, 883 (1972).

[26] A. Regnat, Low-temperature properties and magnetic structure of CrB_2, MnB_2, and CuMnSb, Ph.D. dissertation, Technische Universität München, 2019, https://mediatum.ub.tum.de/1463155.

[27] M. Cadeville, Proprietes magnetiques des diborures de manganese et de chrome: MnB_2 et CrB_2, J. Phys. Chem. Solids **27**, 667 (1966).

[28] S. Neov and E. Legrand, Neutron diffraction study of the magnetic structure of Mn_3B_4, Phys. Status Solidi B **49**, 589 (1972).

[29] M. Cococcioni and S. de Gironcoli, Linear response approach to the calculation of the effective interaction parameters in the LDA + U method, Phys. Rev. B **71**, 035105 (2005).

[30] V. Sokolovskiy, D. Baigutlin, O. Miroshkina, and V. Buchelnikov, Meta-GGA SCAN functional in the prediction of ground state properties of magnetic materials: Review of the current state, Metals **13**, 728 (2023).

[31] R. Nagai, R. Akashi, and O. Sugino, Machine-learning-based exchange correlation functional with physical asymptotic constraints, Phys. Rev. Res. **4**, 013106 (2022).

[32] P. E. Blöchl, Projector augmented-wave method, Phys. Rev. B **50**, 17953 (1994).

[33] G. Kresse and J. Furthmüller, Efficient iterative schemes for ab initio total-energy calculations using a plane-wave basis set, Phys. Rev. B **54**, 11169 (1996).

[34] See Supplemental Material at http://link.aps.org/supplemental/10.1103/PhysRevB.110.094411 for functional tests on various magnetic materials, as well as the discussions on the hardness models. It includes figures of the antiferromagnetic configurations in the Mn-B system, fitted localized Wannier functions, calculated exchange parameters, and the results of spin dynamics simulations, and which includes Refs. [8–14,22,23,30,31,35–55].

[35] J. Sun, A. Ruzsinszky, and J. P. Perdew, Strongly constrained and appropriately normed semilocal density functional, Phys. Rev. Lett. **115**, 036402 (2015).

[36] J. P. Perdew, K. Burke, and M. Ernzerhof, Generalized gradient approximation made simple, Phys. Rev. Lett. **77**, 3865 (1996).

[37] C. Zhou, J. Xing, B. Xiao, J. Feng, X. Xie, and Y. Chen, First principles study on the structural properties and electronic structure of X2B (X = Cr, Mn, Fe, Co, Ni, Mo and W) compounds, Comput. Mater. Sci. **44**, 1056 (2009).

[38] X. Zhao, L. Li, K. Bao, P. Zhu, Q. Tao, S. Ma, and T. Cui, Insight the effect of rigid boron chain substructure on mechanical, magnetic and electrical properties of β-FeB, J. Alloys Compd. **896**, 162767 (2022).

[39] H. Gou, N. Dubrovinskaia, E. Bykova, A. A. Tsirlin, D. Kasinathan, W. Schnelle, A. Richter, M. Merlini, M. Hanfland, A. M. Abakumov *et al.*, Discovery of a superhard iron tetraboride superconductor, Phys. Rev. Lett. **111**, 157002 (2013).

[40] M. Cadeville and E. Daniel, Sur la structure électronique de quelques borures d'éléments de transition, J. Phys. **27**, 449 (1966).

[41] B. Decker and J. Kasper, The crystal structure of TiB, Acta Crystallogr. **7**, 77 (1954).

[42] A. Knappschneider, C. Litterscheid, D. Dzivenko, J. A. Kurzman, R. Seshadri, N. Wagner, J. Beck, R. Riedel, and B. Albert, Possible superhardness of CrB4, Inorg. Chem. **52**, 540 (2013).

[43] S. Calder, B. Saparov, H. B. Cao, J. L. Niedziela, M. D. Lumsden, A. S. Sefat, and A. D. Christianson, Magnetic structure and spin excitations in $BaMn_2Bi_2$, Phys. Rev. B **89**, 064417 (2014).

[44] Y. Singh, M. A. Green, Q. Huang, A. Kreyssig, R. J. McQueeney, D. C. Johnston, and A. I. Goldman, Magnetic order in $BaMn_2As_2$ from neutron diffraction measurements, Phys. Rev. B **80**, 100403(R) (2009).

[45] Z. Yamani, Z. Tun, and D. Ryan, Neutron scattering study of the classical antiferromagnet MnF_2: A perfect hands-on neutron scattering teaching course, Can. J. Phys. **88**, 771 (2010).

[46] R. Toft-Petersen, N. H. Andersen, H. Li, J. Li, W. Tian, S. L. Bud'ko, T. B. S. Jensen, C. Niedermayer, M. Laver, O. Zaharko *et al.*, Magnetic phase diagram of magnetoelectric $LiMnPO_4$, Phys. Rev. B **85**, 224415 (2012).

[47] A. M. Arévalo-López and J. P. Attfield, Weak ferromagnetism and domain effects in multiferroic LiNbO 3-type MnTiO 3-II, Phys. Rev. B **88**, 104416 (2013).

[48] C. Autret, C. Martin, M. Hervieu, R. Retoux, B. Raveau, G. Andre, and F. Bourée, Structural investigation of Ca_2MnO_4 by neutron powder diffraction and electron microscopy, J. Solid State Chem. **177**, 2044 (2004).

[49] Y. F. Guo, A. J. Princep, X. Zhang, P. Manuel, D. Khalyavin, I. I. Mazin, Y. G. Shi, and A. T. Boothroyd, Coupling of magnetic order to planar Bi electrons in the anisotropic Dirac metals $AMnBi_2$ (A = Sr, Ca), Phys. Rev. B **90**, 075120 (2014).

[50] G. Cordier and H. Schäfer, Darstellung und Kristallstruktur von $BaMnSb_2$, $SrMnBi_2$ und $BaMnBi_2$ /Preparation and Crystal Structure of $BaMnSb_2$, $SrMnBi_2$ and $BaMnBi_2$, Z. Naturforsch. B **32**, 383 (1977).

[51] X. Guo, L. Li, Z. Liu, D. Yu, J. He, R. Liu, B. Xu, Y. Tian, and H.-T. Wang, Hardness of covalent compounds: Roles of metallic component and d valence electrons, J. Appl. Phys. **104**, 023503 (2008).

[52] P. C. Müller, C. Ertural, J. Hempelmann, and R. Dronskowski, Crystal orbital bond index: Covalent bond orders in solids, J. Phys. Chem. C **125**, 7959 (2021).

[53] D. M. Teter, Computational alchemy: The search for new superhard materials, MRS Bull. **23**, 22 (1998).

[54] X.-Q. Chen, H. Niu, D. Li, and Y. Li, Modeling hardness of polycrystalline materials and bulk metallic glasses, Intermetallics **19**, 1275 (2011).

[55] Y. Tian, B. Xu, and Z. Zhao, Microscopic theory of hardness and design of novel superhard crystals, Int. J. Refract. Hard Met. **33**, 93 (2012).

[56] M. Methfessel and A. T. Paxton, High-precision sampling for Brillouin-zone integration in metals, Phys. Rev. B **40**, 3616 (1989).
[57] V. L. Deringer, A. L. Tchougreeff, and R. Dronskowski, Crystal orbital Hamilton population (COHP) analysis as projected from plane-wave basis sets, J. Phys. Chem. A **115**, 5461 (2011).
[58] X. He, N. Helbig, M. J. Verstraete, and E. Bousquet, TB2J: A python package for computing magnetic interaction parameters, Comput. Phys. Commun. **264**, 107938 (2021).
[59] A. A. Mostofi, J. R. Yates, Y.-S. Lee, I. Souza, D. Vanderbilt, and N. Marzari, Wannier90: A tool for obtaining maximally-localised Wannier functions, Comput. Phys. Commun. **178**, 685 (2008).
[60] R. F. Evans, W. J. Fan, P. Chureemart, T. A. Ostler, M. O. Ellis, and R. W. Chantrell, Atomistic spin model simulations of magnetic nanomaterials, J. Phys.: Condens. Matter **26**, 103202 (2014).
[61] A. Lawson, A. C. Larson, M. Aronson, S. Johnson, Z. Fisk, P. Canfield, J. Thompson, and R. Von Dreele, Magnetic and crystallographic order in α-manganese, J. Appl. Phys. **76**, 7049 (1994).
[62] K. Lejaeghere, V. Van Speybroeck, G. Van Oost, and S. Cottenier, Error estimates for solid-state density-functional theory predictions: An overview by means of the ground-state elemental crystals, Crit. Rev. Solid State **39**, 1 (2014).
[63] A. Pulkkinen, B. Barbiellini, J. Nokelainen, V. Sokolovskiy, D. Baigutlin, O. Miroshkina, M. Zagrebin, V. Buchelnikov, C. Lane, R. S. Markiewicz *et al.*, Coulomb correlation in non-collinear antiferromagnetic α-Mn, Phys. Rev. B **101**, 075115 (2020).
[64] T. Şimşek, T. Şimşek, and Ş. Özcan, Synthesis and characterization of Mn_2B nanocrystals by mechanical alloying method, J. Boron **4**, 25 (2019).
[65] P. Mohn, The calculated electronic and magnetic properties of the tetragonal transition-metal semi-borides, J. Phys.: Condens. Matter **21**, 2841 (1988).
[66] H. Okamoto, B-Mn (boron-manganese), J. Phase Equilib. **14**, 121 (1993).
[67] L.-E. Tergenius, Refinement of the crystal structure of orthorhombic Mn_2B (formerly denoted Mn4B), J. Less Common Met. **82**, 335 (1981).
[68] D. Wang, L. Ma, L. Li, X. Xu, Y. Guo, and S. Zhao, Characterization of polycrystalline Fe 2 B compound with high saturation magnetization, J. Supercond. Nov. Magn. **31**, 431 (2018).
[69] S. Klemenz, M. Fries, M. Dürrschnabel, K. Skokov, H.-J. Kleebe, O. Gutfleisch, and B. Albert, Low-temperature synthesis of nanoscale ferromagnetic α'-MnB, Dalton Trans. **49**, 131 (2020).
[70] S. Kervan, Magnetic properties of the MnB boride by density functional theory, J. Supercond. Nov. Magn. **24**, 815 (2011).
[71] N. Kalyon, A.-M. Zieschang, K. Hofmann, M. Lepple, M. Fries, K. P. Skokov, M. Dürrschnabel, H.-J. Kleebe, O. Gutfleisch, and B. Albert, CrB-type, ordered α-MnB: Single crystal structure and spin-canted magnetic behavior, APL Mater. **11**, 060701 (2023).
[72] J. D. Bocarsly, E. E. Levin, S. A. Humphrey, T. Faske, W. Donner, S. D. Wilson, and R. Seshadri, Magnetostructural coupling drives magnetocaloric behavior: The case of MnB versus FeB, Chem. Mater. **31**, 4873 (2019).
[73] H. Hirota and A. Yanase, Magnetic properties of Mn_3B_4, J. Phys. Soc. Jpn. **20**, 1596 (1965).
[74] Y. An, J. Li, K. Wang, G. Wang, S. Gong, C. Ma, T. Wang, Z. Jiao, X. Dong, G. Xu *et al.*, Superconductivity and topological properties of MgB_2-type diborides from first principles, Phys. Rev. B **104**, 134510 (2021).
[75] S. Khmelevskyi and P. Mohn, Magnetic ordering in MnB_2: An ab initio study, Solid State Commun. **113**, 509 (2000).
[76] A. Knappschneider, C. Litterscheid, J. Brgoch, N. C. George, S. Henke, A. K. Cheetham, J. G. Hu, R. Seshadri, and B. Albert, Manganese Tetraboride, MnB_4: High-temperature crystal structure, p–n Transition, 55Mn NMR spectroscopy, solid solutions, and mechanical properties, Chem. Eur. J. **21**, 8177 (2015).
[77] A. Knappschneider, C. Litterscheid, N. C. George, J. Brgoch, N. Wagner, J. Beck, J. A. Kurzman, R. Seshadri, and B. Albert, Peierls-distorted monoclinic MnB_4 with a Mn Mn Bond, Angew. Chem. Int. Ed. Engl. **53**, 1684 (2014).
[78] N. Steinki, J. Winter, D. S. Grachtrup, D. Menzel, S. Süllow, A. Knappschneider, and B. Albert, Electronic and magnetic ground state of MnB_4, J. Alloys Compd. **695**, 2149 (2017).
[79] Y. Liang, X. Yuan, Y. Gao, W. Zhang, and P. Zhang, Phonon-assisted crossover from a nonmagnetic Peierls Insulator to a magnetic Stoner metal, Phys. Rev. Lett. **113**, 176401 (2014).
[80] Y. Liang, P. Qin, H. Jiang, L. Zhang, J. Zhang, and C. Tang, Designing superhard metals: The case of low borides, AIP Adv. **8**, 045305 (2018).
[81] G. Akopov, L. E. Pangilinan, R. Mohammadi, and R. B. Kaner, Perspective: Superhard metal borides: A look forward, APL Mater. **6**, 070901 (2018).
[82] J. Haines, J. M. Léger, and G. Bocquillon, Synthesis and design of superhard materials, Annu. Rev. Mater. Res. **31**, 1 (2001).
[83] Q. Wang, J. He, W. Hu, Z. Zhao, C. Zhang, K. Luo, Y. Lü, C. Hao, W. Lü, and Z. Liu, Is orthorhombic iron tetraboride superhard? J. Materiomics **1**, 45 (2015).
[84] M. Zhang, M. Lu, Y. Du, L. Gao, C. Lu, and H. Liu, Hardness of FeB_4: Density functional theory investigation, J. Chem. Phys. **140** (2014).
[85] D. Pettifor, Theoretical predictions of structure and related properties of intermetallics, Mater. Sci. Technol. **8**, 345 (1992).
[86] W. Hume-Rothery, C. W. Haworth, and R. E. Smallman, *The Structure of Metals and Alloys*, 5th ed. (Institute of Metals and the Institution of Metallurgists, London, 1969).
[87] J. Santiago, C. Huang, and E. Morosan, Itinerant magnetic metals, J. Phys.: Condens. Matter **29**, 373002 (2017).
[88] T. Şimşek and Ş. Özcan, Influence of crystal size on the magnetic properties of manganese monoboride nanoparticles, IEEE Trans. Magn. **54**, 2301204 (2018).
[89] P. Rhodes and E. P. Wohlfarth, The effective Curie-Weiss constant of ferromagnetic metals and alloys, Proc. R. Soc. London A: Math. Phys. Sci. **273**, 247 (1963).
[90] N. D. Mermin and H. Wagner, Absence of ferromagnetism or antiferromagnetism in one-or two-dimensional isotropic Heisenberg models, Phys. Rev. Lett. **17**, 1133 (1966).

Correction: The affiliation indicators for the last author were not presented properly during the production cycle and have been corrected.